The Cryosphere Discuss., https://doi.org/10.5194/tc-2017-127
Manuscript under review for journal The Cryosphere
Discussion started: 28 July 2017
© Author(s) 2017. CC BY 4.0 License.

The Cryosphere Discussions
Open Access
EGU

Estimation of Degree of Sea Ice Ridging Based on Dual-Polarized C-band SAR Data

Alexandru Gegiuc, Markku Similä, Juha Karvonen, Mikko Lensu, Marko Mäkynen, and Jouni Vainio
Finnish Meteorological Institute(FMI), Marine Research, Erik Palménin aukio 1, 00560 Helsinki, Finland
Correspondence to: Alexandru Gegiuc (alexandru.gegiuc@fmi.fi)

Abstract.

For navigation in Baltic Sea ice during winter season, parameters such as ice edge, ice concentration, ice thickness, ice drift and degree of ridging are usually reported daily in the manually prepared Ice Charts, which provide icebreakers essentail information for route optimization and fuel calculations. However, manual ice charting requires long analysis times and detailed analysis is not possible for large scale maps (e.g. Arctic Ocean). Here, we propose a method for automatic estimation of degree of ridging density in the Baltic Sea region, based on RADARSAT-2 C-band dual-polarized (HH/HV channels) SAR texture features and the sea ice concentration information extracted from the Finnish Ice Charts. The SAR images were first segmented and then several texture features were extracted for each segment. Using the Random Forest classification, we classified them into four classes of ridging intensity and compared them to the reference data extracted from the digitized Ice Charts. The overall agreement between the ice chart based degree of ice ridging (DIR) and the automated results varied monthly, being 83 %, 63 % and 81 % in January, February and March 2013, respectively. The correspondence between the degree of ice riding of the manual Ice Charts and the actual ridge density was good when this issue was studied based on an extensive field campaign data in March 2011.

1 Introduction

Navigation in sea ice is naturally hampered by rapid changes in the environmental conditions. Thus, it is essential for winter time shipping and off-shore operations to get reliable and up-to-date information on the prevailing ice conditions. The most important sea ice related information are the location of the sea ice edge, sea ice types, sea thickness and concentration and sea ice deformation. Without detailed sea ice information, navigating through heavily ridged sea ice is very difficult and time consuming or even impossible.

The Baltic Sea is a semi-enclosed brackish sea water basin in Northern Europe. The ice cover in the Baltic Sea usually begins to form in November, and has its largest extent between January and March, Seina and Peltola (1991). The normal ice break-up starts in April and the ice melts completely by the beginning of June. The maximum annual ice cover ranges from 12% to 100% of the whole Baltic Sea area, and the average is 40%, Seina and Palosuo (1996). During the last decades there has prevailed a clear decreasing trend in the maximum ice extent although the trend has not been a subject for a detailed investigation. The sea ice in the Baltic Sea can be divided into fast ice and drift ice. Fast ice appears in the coastal and archipelago areas. Drift

The Cryosphere Discuss., https://doi.org/10.5194/tc-2017-127
Manuscript under review for journal The Cryosphere
Discussion started: 28 July 2017
© Author(s) 2017. CC BY 4.0 License.

ice has a dynamic nature due to forcing by winds and currents. The motion of drift ice results in an uneven and broken ice field with distinct floes up to several kilometers in diameter, leads and cracks, brash ice barriers, rafted ice and ice ridges. The upper limit for thermodynamically grown ice is 70 cm or less during most winters, Palosuo et al. (1982). The thickness of ice ridges is typically 5 to 15 m, Lepparanta and Hakala (1992). The salinity of the Baltic Sea ice is typically from 0.2 to 2 ‰ depending on the location, time, and weather history, Hallikainen (1992). Synthetic Aperture Radar (SAR) satellites such as RADARSAT-2 (RS-2) and Sentinel-1 (S-1) play a major role in operationally monitoring the ice conditions in Baltic Sea every winter. SAR imaging is practically independent of the atmosphere conditions (e.g. cloud cover) and solar illumination, and thus, can be used in continuous automated sea ice monitoring . However, radar backscatter information in the SAR imagery cannot easily be directly linked to the different ice types or ice properties at a given location, and the expertise of an trained ice analyst is then required.

In the Baltic Sea, daily ice charts prepared by the Finnish Ice Service (FIS) analysts in winter time provide a daily source of information upon the ice conditions by assigning a classification of ice types and other ice properties to the ice chart polygons descibed by well-defined symbols and coloring of the polygons. They are based on visual interpretation of the SAR imagery as the principal source of ice information. Currently, RS-2 and S-1 SAR imagery with a wide coverage (e.g. RS-2 ScanSAR Wide Mode with 500 by 500 km image size) are used. The SAR imagery is complemented by visible and thermal infrared imagery from Moderate Resolution Imaging Spectroradiometer (MODIS), in-situ observations, sea ice information messages from icebreakers, and data from sea ice models.. The ice chart polygons are defined by the ice analysts and they represent uniform ice areas with similar ice parameters. Parameters assigned for each polygon are ice concentration, level ice thickness range and average, and the the degree of ice ridging (DIR). The FIS ice analysts estimate the DIR category mainly using the SAR imagery, and with additional information on the ice drift based on successive SAR images and results of sea ice models (Figure 1). The main criteria for the visual DIR estimation from the SAR imagery are the SAR backscattering and its visible patterns (SAR texture). Because the visual interpretation is so essentail in the manual ice charting process, a certain amount of subjectivity and inconsistency by different ice analysts is inevitable.

In this paper we propose an automation of the DIR estimation process based on RadarSat-2 dual-polarized (HH/HV) C-band SAR data using data acquired under cold conditions during the winter season 2012-2013 and using the FIS Ice Charts as reference data. In Section 2.1 we will discuss on the different DIR categories used by FIS. As a tool in the DIR classification we use the Random Forest (RF) algorithm which will explained in detail in Section 3.3. Using the automated classification procedure we target to an efficient exploitation of the RS-2 SAR data and an improved quality (pixel level accuracy and consistency between different analysts) of the ice charts, by means of increased spatial and temporal resolutions.

Under cold weather conditions when the snow cover on sea ice is dry the ice surface scattering has been observed to be the dominant component in the total co-polarized backscattering measured by radars operating at C-band with incidence angles below 45°, Carlström and Ulander (1995); Dierking et al. (1999). If the ice surface is very smooth and salinity < 0.5 psu, which typically is the case for level fast ice in the Baltic Sea, and the backscattering from ice-water interface and ice volume is significant. The surface backscattering from level ice is controlled by the statistics of the small-scale roughness as well as the salinity of the ice surface. If sea ice is deformed, the large-scale surface roughness alters the geometry of the surface and, hence,

The Cryosphere Discuss., https://doi.org/10.5194/tc-2017-127
Manuscript under review for journal The Cryosphere
Discussion started: 28 July 2017
© Author(s) 2017. CC BY 4.0 License.

also modifies the backscattering. Empirical measurements of the Baltic Sea C-band SAR ice backscattering coefficient (σ^o) have shown that the variation in the large-scale surface roughness mostly modulates σ^o and image texture although changes in the small-scale roughness are also significant, Carlström and Ulander (1995); Dierking et al. (1999); Mäkynen et al. (2004).

The σ^o contrast between level ice and deformed ice is on average larger at C-band cross-polarization than at co-polarization, Mäkynen et al. (2004). The standard deviation of σ^o was observed to be larger for deformed ice types (mixtures of level ice, ice ridges, rubble) than for level ice types and brash ice in Mäkynen et al. (2004). Radar backscatter in C-band SAR imagery is not directly related to the sea ice thickness, but at least in the Baltic Sea it is possible to estimate the thickness of deformed ice under dry snow conditions through a statistical relationship between ice freeboard, level ice thickness and σ^o, Similä et al. (2010). The variance of the mean freeboard, i.e. large scale surface roughness, increases with increasing average freeboard, and as the surface roughness increases σ^o also typically increases. In general, these previous studies on sea ice σ^o signatures have shown that there is a relation between C-band σ^o and DIR, but further studies are needed to better quantify this relation.

Many sea ice classification systems just perform classification to open water and different ice types, such as new ice, first-year-ice, multiyear-ice, but DIR is not explicitly estimated in more detail. Classification schemes utilizing σ^o and SAR texture have been presented e.g. in Soh (2004); Sandven et al. (2012); Barber et al. (1991); Clausi (2001). A progressive scheme presented e.g. in Soh (2004) utilizes segmentation and multiple segment-wise features, including texture. Classification of ice types based on single-polarization C-band SAR backscattering has been studied e.g. in Karvonen (2004); Shokr (2009). In Soh (1999) the performance of texture measures based on Gray Level Co-Occurrence Matrices (GLCM's) were studied for sea ice classification into seven classes, which were based on human visual inspection. Sea ice SAR classification using the world meteorological organization (WMO) ice categories (stage of development) WMO (2010) has been studied e.g. in Clausi (2001); Deng and Clausi (2005); Maillard et al. (2005); Yu and Clausi. (2007); Clausi (2010); Ochilov et al. (2012). These approaches are based on SAR segmentation and different SAR features, including texture ones. Some of the methods also combine the ice analyst analysis and an automated analysis. A system capable of a semi-automated segmentation and enhanced classification with a digitized ice chart as an input is presented in Clausi (2010). The ice categories in these studies do not either explicitly or uniquely include DIR classification.

2 Data Sets and Processing

The Baltic Sea ice season 2012/2013 was average but the turning point of the winter was late. The weather began to cool off at the end of the first week of January and the extent of ice increased. In the last week of January the strong winds moved the ice fields and the mild weather melted ice. In the beginning of February the weather continued similar – at night new ice was formed which the winds then broke during the day. Towards the end of February the weather cooled down and new ice was formed also in the Gulf of Finland. In the beginning of March cold arctic air started to flow to Scandinavia and the extent of ice began to grow. The whole March was extremely cold. In the 15th of March the extent of ice reached 177 000 km², which was the maximum of the ice winter. From then on the cold nights formed new ice but sunny days melted them and the extent of the sea ice did not increase any more.

The Cryosphere Discuss., https://doi.org/10.5194/tc-2017-127
Manuscript under review for journal The Cryosphere
Discussion started: 28 July 2017
© Author(s) 2017. CC BY 4.0 License.

2.1 Ice charts and degree of ridging

Our reference data set consists of the daily FMI FIS manual ice charts over the Baltic Sea. In the ice charts the degree of ice ridging (DIR) is used to categorise ice types in a way that is relevant for the difficulty of navigation. DIR is assigned as a qualitative numeral, ranging from 1 to 5, to each ice chart polygon. DIR value 1 refers to level ice or rafted ice. Small ridged areas in the middle of level ice are also included into DIR 1. Values 2 and 3 represent lightly ridged ice and ridged ice, respectively. The most heavily ridged ice is assigned DIR value 4. DIR 5 indicates brash barrier while this particular category was not present in our data set. By visual inspection of the RS-2 and S-1 SAR wide swath imagery with a spatial resolution of approximately 100m resolution it is not possible to describe the ridging intensity quantitatively. However, it is feasible to assign categories of ridged ice for extended areas for which the actual ridging intensities differ. For some justification of the meaningfulness of the areal DIR values see our comparison with the 2011 field data set in Section 4.1.

The DIR information in the FIS ice charts is typically reported for rather large areas (hundreds of square kilometers) with usually incomplete spatial and temporal accuracy as the ice charts are issued only once daily in the afternoon and are based on the information gathered since the previous afternoon. Consequently, fresh SAR imagery with updated sea ice conditions can often be disregarded if acquired soon after the ice chart has been released for a particular day, and thus the ice chart may become outdated compared to SAR imagery.

The ice charts are also saved as numerical grids from the ice charting software. For the gridded product they are digitized into grids with a resolution of approximately 1 nautical mile (NM). In the grid format the ice thickness, ice concentration and DIR value assigned to each ice chart polygon are included. Additionally the sea surface open water surface temperature is included in the ice chart grids. This practice slightly differs from the classes defined by the ice charting guidelines in Canadian Ice Service, MANICE (2005), where the ice is classified based on the stage of development and indicated by the so-called WMO egg codes, WMO (2010).

No long-term studies between ice chart degrees of ice ridging and the actual ridging statistics have been carried out although field campaigns to measure ridging in the Bay of Bothnia started already in late 1970's by shipborne laser profilers and the first extensive airborne laser profiler campaign was conducted in 1988, see Lewis et al. (1993). Results from three other campaigns in the 1993, 1994 and 1997 are summarised in Lensu (2003). The campaign results discussed in this paper are from a campaign on 2-7 March 2011 with approximately 600 km of measurement lines. Then the measurements were collected by a helicopterborne electromagnetic (HEM) device which combines laser profiling and inductive distance measurement to the ice-water interface. Hence, the HEM measurements give a as comprehensive understanding on ridging as is obtainable from linear profiles. They provide the total thickness and the horizontal resolution of the EM instrument is also sufficient for resolving ridge keels, Haas et al. (2009). The ice season 2010-2011 was severe, with a maximum ice extent of 309 000 km^2. In the Bay of Bothnia mid–basin pack the level ice thicknesses reached 60 cm which somewhat decreased ridging from what would have been expected during an average winter with similar wind conditions. The ridging generally intensified towards the northwestern part of the Bay of Bothnia and towards fast ice edge, and there were coastal rubble fields generated by the closing of flaw leads covered by thinner ice.

The Cryosphere Discuss., https://doi.org/10.5194/tc-2017-127
Manuscript under review for journal The Cryosphere
Discussion started: 28 July 2017
© Author(s) 2017. CC BY 4.0 License.

2.2 SAR image mosaics

The SAR imagery used in this study were RADARSAT-2 ScanSAR wide Wide (SCWA) dual-polarized imagery with the HH/HV polarization combination. The nominal size of an RS-2 SCWA image is around 500 by 500 km, and the pixel size is 50 m. The spatial resolution is around 73-163 m by 100 m (range by azimuth). The incidence angle (θ^o) varies from 20 to 49 degrees. The equivalent number of looks (ENL) is some larger than six. The noise equivalent σ^o at both HH- and HV-polarisation is around -28 $\pm$ 2.5 dB and the absolute accuracy of σ^o is better than 1 dB MDA (2014).

The acquired RS-2 SAR imagery covered the whole Baltic Sea ice season in 2012-2013, with a total number of 538 SAR images between December 7 2012 and April 16 2013. The amount of SAR images during the test period from January to March was 342, i.e. on average over three SAR scenes per day. For our test period we selected the months during which the SAR images were mostly acquired under dry snow conditions. Hence the dominant backscattering source was the sea ice surface and we could expect a statistical relationship between σ^o and DIR as reported in Carlstr¨om and Ulander (1995); Dierking et al. (1999); Similä et al. (2001); Mäkynen et al. (2004); Similä et al. (2010). Because the ice conditions in the northern parts of the Baltic Sea were the most severe, we restricted our study area to northward from the latitude of 61°N, covering the entire Bay of Bothnia and largely the Sea of Bothnia.

The preprocessing of the RS-2 SCWA images consisted of calibration (calculation of σ^o_{HH} and σ^o_{HV}), georectification, calculation of the incidence angle θ^o, and land masking. First the data were rectified into the Mercator projection in 100 m resolution. This georectification is compatible with the navigation system of the Finnish and Swedish icebreakers. In this Mercator projection the reference latitude is 61 degrees 40 min (N).

As the SAR σ^o is dependent on θ^o, an incidence angle correction is necessary before the classification of the SAR images with wide θ^o range, such as RS-2 SCWA images. For the HH-polarization images, an incidence angle correction method described in Mäkynen et al. (2002) was applied. This incidence angle correction maps the σ^o values using a linear dependence for the σ^o in dB-scale to a predefined θ^o value θ^0_R. In this case, the fixed θ^o_R of 30° was used. At the HV-band the SAR backscattering coefficient values are close to the instrument noise floor (around -28 dB for RS-2 ScanSAR Wide mode), and the noise floor (noise equivalent σ^o) varies along the across-track direction. The noise floor modulates the (low) HV channel signal leading to clearly visible stripes (artifacts) at HV band. These stripes complicate both the visual and automated interpretation of the SAR data. We applied a statistical noise reduction procedure at the RS-2 HV channel. The procedure is described in detail in Karvonen (2015).

The rectified and incidendence angle corrected images were land masked. The land masking was based on the GSHHG (Global Self-Consistent Hierarchical, High-resolution Geography database from the National Oceanic and Atmospheric Administration, NOAA) coastline data, Wessel and Smith (1996).

Then the SAR images were segmented and the segmentwise features were calculated in the resolution of 100 m, for details see Sections 3.1 and 3.2. Due to the large size of SAR images the HH and HV images and also the feature images were downsampled into 500 m resolution. The daily SAR mosaics were constructed after receiving the morning RS-2 image acquisitions such that the most recent imagery is overlaid the older imagery. The test area was typically covered by RS-2 every 1 to 2 days.

The Cryosphere Discuss., https://doi.org/10.5194/tc-2017-127
Manuscript under review for journal The Cryosphere
Discussion started: 28 July 2017
© Author(s) 2017. CC BY 4.0 License.

Delays up to two days are possible, however, usually the delays in the test area are one day or less. The SAR mosaics always represented the latest SAR information at each location.

The equivalent number of looks (ENL), noise equivalent σ^o and autocorrelation between neighboring pixels in the rectified images were studied using homogeneous areas of size 3.1x3.1 km visually selected from the images over open water areas with a weak texture. The ENL was around 9.5 for the whole θ^o range as the resolution 100 m. Thus, the radiometric resolution was around 1.2 dB and the standard deviation (std) of fading was 1.4 dB. The autocorrelation coefficient between the adjacent 100 m pixels was on average only 0.18.

2.3 Correspondence between ice charts and SAR mosaics

We found that often the ice charts did not correspond to the SAR mosaics of the same day. This has occurred because some part of the daily SAR mosaic was a few of days old or because the SAR mosaic was updated after the preparation of the manual ice chart. We note that FIS also uses MODIS data when producing a new ice chart. Due to the inconsistencies between ice charts and SAR data we examined every DIR chart during the whole test period from the 1 January to 31 March and compared them visually to the corresponding SAR mosaic.

This process resulted in the rejection of many of the ice charts during the test period. In our analysis we included only those days in which the DIR charts appeared to be in overall agreement with the corresponding SAR mosaics. There were 10 such ice charts in January, 15 in February and 12 in March.

3 Methodology for estimation of the degree of ice ridging

3.1 SAR Image segmentation

In order to perform the segmentation we combined the HH- and HV-polarized RS-2 SCWA images data using the Principal Component Analysis (PCA) technique. PCA is a statistical procedure that uses an orthogonal transformation to convert an image of possibly correlated pixel values into an image of linearly uncorrelated pixels. The values of these pixels are called principal component scores. We selected the first PCA image (corresponding to the largest PCA eigenvalue) for the segmentation because it explains most of the variation contained in the HH- and HV-images. This allowed us to speed up the segmentation which for large SAR data sets requires a considerable amount of time and computing resources.

For data segmentation, there are many algorithms available, but very few that can work well with SAR imagery because of the small dynamic σ^0 range, [-22, - 7] dB is typical HHl SAR C-band images and [-28, - 24] dB for HV images. There does not exist a clear separation between different sea ice types based on the magnitude of σ^0 , and the presence of the speckle complicates the segmentation task further. In the segmentation we truncated the HH range to [-22, - 8] dB. Here, the first PCA image from the HH- and HV-polarization SAR imagery was segmented with a Markov Random Field approach, Rue et al. (2005), and optimized with an Modified Metropolis Dynamics algorithm, similar as in Kato et al. (1992, 1994); Berthod et al. (1996). This stochastic method has been demonstrated to provide a better segmentation than a deterministic one, e.g. Iterated

The Cryosphere Discuss., https://doi.org/10.5194/tc-2017-127
Manuscript under review for journal The Cryosphere
Discussion started: 28 July 2017
© Author(s) 2017. CC BY 4.0 License.

Conditional Mode (ICM) by Besag (1974)), for typical sea ice SAR imagery, Ochilov et al. (2012); Deng and Clausi (2004, 2005). Markov Random Field (MRF) approach relies less on the initial segmentation, and also takes into account the global and local statistics of a pixel. This guarantees that pixels with similar intensities would not be treated in the same way in different regions of an image I, if the local spatial interactions differ in the two regions.

For example, to select the best new label $\hat{L}$ for a group of neighborhood pixels (cliques) in a site s, is equivalent to maximize the probability distribution of labels in site s, conditioned by the a-priori label (L). In other words, $\hat{L}_{MAP} = argmax_{L\in\Omega} P(L|F=f)$. where Ω is the set of labels, $(F=f)$ is feature vector, (L) is the segmented result conditioned by the feature vector. For each s, the cliques potential depends on the local configuration and type (size, shape, and possibly orientation). For simple cliques (formed by the closest neighbored pixels), their potential function V_c can be reduced to only two states:

$$V_c(L) = \beta\delta(L_i, L_j) = +1 if L_i = L_j; -1 if L_i \neq L_j. \tag{1}$$

The site's energy would simply be the sum of all cliques potential:

$$U(L) = \sum_{c\in C} V_c(L). \tag{2}$$

For more complex cliques (higher order neighbours), their potential would depend on the computed local mean (μ_{L_s}) and variance ($\sigma^2_{L_s}$). The labels (classes) would then be represented by Gaussian distributions:

$$P(f_s|L_s) = \frac{1}{\sqrt{2\pi}\sigma_{L_s}} \exp\left(\frac{-(f_s-\mu_{L_s})^2}{2\sigma^2_{L_s}}\right) \tag{3}$$

If we consider the probability distribution of labels in s a Markov Random Field with $P(L|F=f) > 0$, we can also treat it as a Gibbs form Besag (1974) :

$$P(L) = \frac{1}{Z} exp(-\sum_{c\in C} V_c(L)), \tag{4}$$

where Z is the normalization constant and $V_c(L)$ is the clique's potential for the current label state.

For this example the (logarithmic) energy is

$$U(L) = \sum_{S} (\log((2\pi)^{1/2}\sigma_{L_s}) + \frac{(f_s-\mu_{L_s})^2}{2\sigma^2_{L_s}} + \sum_{s,r} \beta\delta(w_s, w_r), \tag{5}$$

where the homogenity of the region is controlled by the β parameter. and

$$P(L|F=f) = \frac{1}{Z}\exp(-U(L)) \rightarrow \hat{L}_{MAP} = \text{argmax}_L P(L|F=f) = \text{argmin}_L U(L). \tag{6}$$

These kind of functions can then be optimized by various methods, one being the simulated annealing method Kirkpatrick (1983), Cerny (1985), where a slow decrease in the probability of accepting worse solutions occurs as the algorithm searches the solution space. The method used here is an adaptation of the Metropolis-Hastings algorithm introduced in Metropolis et al.

© Author(s) 2017. CC BY 4.0 License.

(1953) or shortly Metropolis algorithm which was created as a Monte Carlo method to generate sample states of a thermodynamic system. In the algorithm the labeling is also dependent on the control variable called temperature T. If the energy function U(L) value increases, the label is changed with a probability dependent on T and increase of U(L) ($\exp(-\Delta U/T)$).

To perform the MRF segmentation, we first need to initialize the Gaussian parameters for the labels and also the number of labels. This is performed automatically for each SAR image separately. First the histogram of the SAR image is computed, and then the Expectation-Maximization (EM), Dempster et al. (1977), algorithm is applied to decompose the histogram into a Gaussian decomposition. The number of Gaussians in the decomposition is initialized to a small minimum value, e.g. two, and then iteratively increased until the EM decomposition and the histogram are similar enough with each other. We measure the similarity by the coefficient of correlation r. We stop the EM-algoritm if either r exceeds t 0.97 or if we have more than nine labels in the image. We initially label the image pixels based on the EM classification , i.e. we assign the label with highest probability of the N different Gaussian distributions $G_k(x)$ for a pixel. After this labeling scheme we can run the MRF segmentation.

An example of segmentation result for the Bay of Bothnia is shown in Fig. 2 together with the original HH and HV SAR mosaics.

The next step in the SAR analysis was to compute several SAR quantities for the obtained segments.

3.2 SAR image features

Using the computed SAR features and the DIR values from FMI ice charts we studied the classification of DIR categories for our test period . The following SAR features were computed and their efficiency in DIR classification was studied. Each feature value is a median value of the feature computed over a single segment. Their abbreviations are inside the brackets:

1. HH-band SAR backscattering coefficient (σ^o_{HH}), with incidence angle correction applied.
2. HV-band SAR backscattering coefficient (σ^o_{HV}), with incidence angle correction and noise level equalization applied.
3. HH-band entropy (E_{HH}), computed for the full-resolution SAR (100m) in windows with a radius of 5 pixels.
4. HV-band entropy (E_{HV}) , computed for the full-resolution SAR (100m) in windows with a radius of 5 pixels.
5. HH-band autocorrelation (AC_{HH}), computed for the full-resolution SAR (100m) in windows with a radius of 5 pixels.
6. HV autocorrelation (AC_{HV}), computed for the full-resolution SAR (100m) in windows with a radius of 5 pixels.
7. HH channel coefficient of variation (CV_{HH}), computed in full resolution for windows with a radius of 5 pixels).
8. HV channel coefficient of variation (CV_{HV}), computed in full resolution for windows with a radius of 5 pixels.
9. Edge density for HH channel (ED_{HH}).
10. Edge density for HV channel (ED_{HV}), scaling: $1000 * N_e/A$ (N_e is the number of edge pixels and A is the segment area).

© Author(s) 2017. CC BY 4.0 License.

11. Segment size (SSZ).

12. HH-channel kurtosis (K_{HH}), computed in a window with radius of 5 pixels in the full SAR resolution.

13. HV-channel kurtosis (K_{HV}), computed in a window with radius of 5 pixels in the full SAR resolution.

Additionally we extracted the segment mean of sea ice concentration (SIC) from the FMI ice charts.

Coefficient of variation was computed separately for HH and HV channels as

$$C^V = \frac{\sigma}{\mu}, \tag{7}$$

where σ is the standard deviation over a data window and μ is the mean over the window. Kurtosis is computed as the fourth moment within a data window.

Entropy E Shannon (1948) was computed separately for HH and HV channels as

$$E = -\sum_{k=0}^{255} p_k log^2 p_k, \tag{8}$$

where p_k's are the proportions of each gray tone k within each computation window. Auto-correlation, ac Similä (1994); Karvonen et al. (2005), was computed as

$$C^A(k,l) = \frac{\sum_{ij \in B} (I(i-k, j-l) - \mu_B)(I(i,j) - \mu_B)}{|B|\sigma_B^2}, \tag{9}$$

where $I(k,l)$ is the pixel value at location (k,l). Mean over the directions horizontal, vertical and diagonal directions i.e. $(k,l) = (0,1)$, $(k,l) = (1,0)$, $(k,l) = (1,1)$ and $(k,l) = (1,-1)$ was used to accomplish directional isotropy. The computation window is denoted by B.

Edge density D was computed for each segment (separately for HH and HV channels) after an edge detection by the Canny algorithm Canny (1986) as

$$D = N_e/N, \tag{10}$$

where N_e is the number of edge pixels with a segment and N is the segment size in pixels. The edges can often be regarded as fragments of an ridged area, when the imprints of the individual ridges disappear in the coarse SAR resolution.

In Fig. 3 computed features for an selected area in central Bay of Bothnia on 15 March 2013 are shown. In the selected area highly and heavily ridged areas are present.

3.3 Random forest classification method

After trying several classification methods (local regression, logistic regression, General Additive Regression Model) we found out that the random forest (RF), Breiman (2001), approach produced good enough results to be of practical use. Random forest is an ensemble learning method which can be applied to classification and regression. In RF we artificially generate several

The Cryosphere Discuss., https://doi.org/10.5194/tc-2017-127
Manuscript under review for journal The Cryosphere
Discussion started: 28 July 2017
© Author(s) 2017. CC BY 4.0 License.

training sets from a single training set at our disposal using bootstrapping, grow a classification tree for each individual training set, perform classification for each tree and then aggregate the results. The bootstrap aggregation is called also bagging. This technique is efficient to reduce variance in high-variance predictions in the same manner than taking an average of samples is, Breiman (2001).

For the classification of the daily ice data we divided our data of 37 days, see Section 2.3 , into the training and the test data sets. At least a time gap of three days was required between test and training data to avoid situations where the same SAR scene and the associated features could be present in both the training data and the test data.

In our computations we have used the routines included in the commercial software Matlab.

3.3.1 Description of the algorithm

We outline the RF algorithm and the used notations. The classes are denoted by $C = \{1, \ldots, C\}$ We have a training set $X = \{x_1, \ldots, x_N\}$ where each sample x_i consists of a feature vector f_i and the corresponding class. When we take a bootstrap sample from X, we denote it Z^*. Our bootstrap sample Z^* is of the same size as the original sample, so on average the fraction 63 % of the original samples of X belong to it, the rest being duplicates, Efron and Tibshirani (1993). The samples of X left out from Z^* (about 37% of the samples) are called out-of-bag (OOB) samples.

The classification tree is denoted $T_b(\Theta_b)$ with $b \in \{1, \ldots, B\}$ and it uses Z^* as its training data. Each end node n of $T_b(\Theta_b)$ has a class label which is the most frequent class in that node. The parameter Θ_b characterizes the bth random forest tree in terms of split variables, split points at each node, and terminal node class label. The class label given by $T_b(\Theta_b)$ depends on the feature vector f_i which is used as input for the tree. We denote it $\hat{C}_b(f_i, \Theta_b)$ We generate B bootstrapped training sets and relying on every training set we grow a classification tree $T_b(\Theta_b)$. A classification tree often achieves a rather low bias if it is grown deep with many nodes without pruning, Hastie et. al. (2011) .

The impurity measure is the Gini index G,

$$G = 1 - \sum_{c=1}^{C} p(c|n)^2$$

where $p(c|n)$ is the proportion of the samples that belong to class c at a particular node n. G indicates how dominant the class c is in the subtree after the split. A small Gini index value indicates that the subtree contains predominantly observations from a single class. In the split the feature component of the vector f_i with the smallest Gini index is utilised Ripley. (1996).

In classification we record the classes predicted by the ensemble of B trees for a specific feature vector, and take a majority vote. The most common class is the class predicted by the ensemble. Then the selected class has a smaller uncertainty than a single classification tree, Hastie et. al. (2011), because an average has a smaller variance than a single variable. This is true also for the correlated variables. If B is large enough the random forest algorithm avoids the tendency of over fitting the model which often occurs in the context of the decision trees.

The problem with bagging is that the grown trees are correlated. To reduce this correlation the RF has a randomisation step. When building trees, each time a split in a tree is considered, a random sample of m predictors is chosen as split candidates

The Cryosphere Discuss., https://doi.org/10.5194/tc-2017-127
Manuscript under review for journal The Cryosphere
Discussion started: 28 July 2017
© Author(s) 2017. CC BY 4.0 License.

from the full set of p predictors ($m = 4$ and $p = 8$ here). A new sample of m predictors is taken at each split. This step prevents the same features to dominate every tree.

The flow of the random forest algorithm is described below.

Random forest algorithm for classification

1. For b = 1 to B:
   (a) Draw a bootstrap sample Z^* of size N from the training data.
   (b) Grow a random-forest tree $T_b(\Theta_b)$ to the bootstrapped data, by recursively repeating the following steps for each terminal node of the tree, until the minimum node size is reached.
      i. Select m variables at random from the p variables.
      ii. Determine the best variable and split-point among the m variables using the Gini index.
      iii. Split the node into two daughter nodes.
2. Output the ensemble of trees $\{T_b(\Theta_b)_1^B\}$.

To classify a new feature vector f_n:

Classification: Let $\hat{C}_b(f_n, \Theta_b)$ be the class prediction of the bth random-forest tree. Then $\hat{C}_{rf}^B(f_n)$ = *majority vote* $\{\hat{C}_b(f_n, \Theta_b)\}_1^B$.

3.3.2 Selection of the features

Because an ensemble of trees was used in RF and a large amount of features were utilized, the results were hard to interpret. To analyse the impact of different features on the class estimation the importance measure was used. This measure is implemented as follows. For each tree, the classification error on the OOB portion of the data is computed. This gives the baseline error rate for the tree. Then in the OOB set we randomly permute one feature of the feature vector f_i and simultaneously keep fixed the other features in f_i. We note that the marginal sampling distribution of the picked feature remains the same during the permutation. Then we recalculate the classification error in the OOB set. This classification error is compared to the baseline error. Usually it is larger than the baseline error. The procedure is repeated for every feature separately. The decrease in classification rate as a result of this permuting is averaged over all trees, and is used as a measure of the importance of the chosen feature.

To select the features we run the RF algorithm for several feature combinations and for several different training data sets. The importance of the features as well as the classification accuracy was monitored. This empirical approach lead to the choice of eight features from the computed 13 features, see Section 3.2. We ended up using the following eight features in deter-

The Cryosphere Discuss., https://doi.org/10.5194/tc-2017-127
Manuscript under review for journal The Cryosphere
Discussion started: 28 July 2017
© Author(s) 2017. CC BY 4.0 License.

mining degree of ice ridging classes: HH-band autocorrelation (AC_{HH}), ice concentration (IC), edge density for HH-channel (ED_{HH}), HH-band entropy (E_{HH}), HH-channel kurtosis (K_{HH}), (σ^o_{HH}), HH-channel coefficient of variation (CV_{HH}) and σ^o_{HV}.

In Fig. 4 is shown the relative importance of the different features as measured by their impact on the correct classification of the out-of-bag samples when the training data covered the whole test period. The importance order of features in this data set is: ice concentration, HH-channel kurtosis , σ^o_{HH}, HH-channel edge density , HH-channel autocorrelation , HH-channel entropy, HH-channel coefficient of variation and σ^o_{HV}. If the training data of just one month was used the relative importance order of features varied to some extent. One feature, ice concentration, remained however the most influential single feature in every case. This is comprehensible because when IC was between 80 % and 90 %, it was almost always assigned to the level ice category (DIR=1). The weak importance of σ^o_{HV} is probably due to the relative narrow range of the σ^o_{HV} values.

We conclude the RF section with a short summary on the major advantages of the RF algorithm : i) RF has the ability to describe complex, nonlinear statistical relationships among variables, ii) RF reduces the uncertainty of the obtained estimate, iii) RF reduces the possibility of over fitting.

The greatest weakness in RF is its relatively weak extrapolation property, Hastie et. al. (2011). This property can be seen from the behaviour of the error rates. The RF classifier has a very low training error rate but the error rates increases significantly for the test set.

4 Results

4.1 Ice chart ridging categories vs. measurements

To give us a perspective on how well the ridging categories in the FIS charts describe the actual ridging we here present the field campaign results. The campaigns in 1993, 1994 and 1997 summarised in Lensu (2003) measured surface profile only while the the fourth campaign during the period from 2 to 7 March 2011 profiled as also ice thickness. From surface profile data ridge sails are identified by cutoff height and Rayleigh criterion according to which the shallower of two adjacent sails is counted only when separated by a trough extending below half its height.Choosing a joint ridge sail height cutoff of 0.4 m a large interannual variation is found for the four campaigns consisting of totally 1600 km of measurement line profile. Ridge densities vary from 5.3/km to 26.7/km, while the sail height shows less variation, from 0.58 m to 0.66 m. To the densities affect mostly the windiness of the season, especially during the early stages with thinner ice types are less resistant against deformation. There are regional differences, the densities increasing with the wind fetch towards the NE corner of the basin, and also the coastal ridge fields often have the character of rubble fields with densities up to 100/km. Sail height depends on average thickness characteristics of the basin, and also the presence of snow cover reduces the heights with a value equalling to the snow thickness. However, as a first approximation the sail height for the Bay of Bothnia can be assumed to be 0.2 m above cutoff. In the interpretation of profile data it must be considered that a considerable fraction of ridges fall below the cutoff and that the sail heights may become sampled from shallower sections of the sails. In field campaigns that typically select the highest point of the sail the observed heights are typically 1-3 m and drilled keel depths 5-15 m, Kankaanpää (1997).

The Cryosphere Discuss., https://doi.org/10.5194/tc-2017-127
Manuscript under review for journal The Cryosphere
Discussion started: 28 July 2017
© Author(s) 2017. CC BY 4.0 License.

To establish compatibility with the ice chart and ice model data, which employ a 1x1 nautical mile (NM) grid, the ridging parameters from the helicopterborne electromagnetic (HEM) data were calculated as averages for the cells of the grid. Here the comparison is made between ridge density and total thickness from HEM data and, on the other hand, the degree of ice riding (DIR) of ice chart data. Although somewhat qualitative the DIR indices are estimates made by sea ice specialists and refer to the Lagrangian ice chart regions corresponding to various formation and deformation phases of the ice cover. The reliability or their boundaries is usually high. The DIR value 1, corresponding level and rafted ice categories, had very small coverage in the data, while DIR 2, the category of slightly ridged ice, was not found at all. The comparison is therefore made for the DIR values 3 and 4, or moderately and severely ridged ice. The sail height retrieved by HEM was equal for these categories while a clear difference was found for the ridge densities and total thicknesses, see Table 1. This indicates that such a rough quantification of ridging can be done based on the indices.

A more detailed picture can be obtained from comparisons of Figure 5 between degree of ice ridging and, on the other hand, ridge sail density and total thickness from the HEM campaign. For ridge density the colorbar range is chosen to be from 12.7 to 21.5 or the average densities corresponding to indices 3 and 4 in Table 5 . Thickness colorbar was scaled similarly. Thus all values below the lower averages are blue and all values above higher averages green. Above and below the colorbar range the ridge density has still a wide range of variation as is seen from the histogram of Figure. The basic regional characteristics can be seen in all three datasets, however. The spatial distribution for the degree of ice riding was in a reasonably good agreement with the HEM-retrieved quantities considering the uttermost simplicity of the former. The agreement for the total ice thickness was somewhat better than agreement for the ridge density, which may be related to the fact that a large fraction of riding does not show in the density due to the cutoff. The correspondence of sail density and total thickness was still good however, as is expected from the fact that the ridge size, as measured by sail height, and ridge density show no clear correlation. This indicates that it is possible to derive relevant data on deformed ice thickness from spatially distributed, surface observable density-like ridging characteristics together with climatologically typical values for ridge size. If ridging is close to isotropicity, the length per square km of ridge sail above cutoff is estimable as pi/2 times ridge density, and further estimates on the fractional area covered by sail rubble are obtained from average sail width. The largest differences between the degree of ice riding and HEM quantities were found in the coastal ridge field extending from 64N 23E to SW. Both ridge density and average sail height were lower for this part in comparison with the extension of the same ridge field to NE from the said location. These values were also similar to those found in the mid basin, so the missing separation of this coastal ridge field into two categories apparent from the HEM data is clearly a shortcoming of the ice chart DIR data.

4.2 Monthly backscattering statistics

We concentrated in our analysis in the areas with IC over 80 %. The marginal ice zone (MIZ) is defined to consist of ice areas with IC from 15 % be 80 %, see e.g. Strong (2012). In areas with IC $80-90$ % the amount of open water area is rather high and it affects the backscattering statistics in a complicated manner depending on wind conditions and the spatial distribution of ice floes. Almost all areas with IC in this range belonged to level ice polygons in our data set. The level ice category (DIR=1)

The Cryosphere Discuss., https://doi.org/10.5194/tc-2017-127
Manuscript under review for journal The Cryosphere
Discussion started: 28 July 2017
© Author(s) 2017. CC BY 4.0 License.

covered well over 50 % of all the ice areas during our test period. Because the resolution in the SAR mosaics were 500 m, the averaging of SAR pixels suppressed the fine scale (100 m) variation present especially in the ridged zones.

We first looked how the σ^o_{HH} distribution changed monthly from January to March in the two main ice categories: level ice ($DIR = 1$) and ridged ice ($DIR > 1$), see Fig 6. In the beginning of January level ice appeared mainly near the coast of the Sea of Bothnia and the dominance of mostly thin ice in the Sea of Bothnia continued up to the middle of February whereas in the Bay of Bothnia appeared also ridged ice areas throughout the whole test period. A significant fraction of the level ice pixels had σ^o_{HH} value below -18 dB indicating thin smooth ice. It is well-known that backscattering from thin ice can also generate large σ^o_{HH} values **?**. Also, the presence of the level ice areas with a relatively low SIC ($80 - 90$ %) meant that open water patches affected the level ice backscattering statistics generating both high and low σ^o_{HH} values. The values of level ice σ^o_{HH} above -18 dB were rather evenly distributed in January. The backscattering from ridged ice areas had a large peak at -16.5 dB and most of the remaining pixel values ranged from -16 dB to -12 dB.

In February σ^o_{HH} there still was present a sharp peak around -20 dB in the level ice area indicating very thin ice but most of σ^o_{HH} values had spread between -16 dB and -11 dB. In the ridged areas a majority of σ^o_{HH} values were in the range between -17 dB and -12 dB. The mean and median values of σ^o_{HH} for level ice areas and ridged areas were almost identical in January and February. In March the backscattering statistics for level and ridged areas showed a clearer discrepancy. The level ice σ^o_{HH} values were distributed rather evenly from -20 dB to -10 dB whereas the σ^o_{HH} values from ridged areas were concentrated in the range from -15 dB to -11 dB. The average value from the ridged areas was over 2 dB higher than that of the level ice areas unlike in the previous months. There was a significant increase in the magnitude of σ^o_{HH} from ridged areas whereas this was not the case for the level ice σ^o value distribution.

Based on Fig. 6 it was obvious that the magnitude of σ^o_{HH} alone could not be an efficient predictor in the estimation of the DIR value in January and February. We reached the same conclusion also in Section 3.3.2 when using the importance of feature measure in the connection with the RF classifier.

We assume that the small separation in the σ^o_{HH} values originating from level ice and deformed ice during the first two test months was due to two major reasons. As mentioned earlier the level ice areas had mostly IC less than 90%. So the backscattering from open water had a significant role in the case of level ice. In addition the level ice area ($DIR = 1$) had significant uncertainties in the FMI charts . The ice analysts responsible for the charts told us that in several cases it was difficult, nearly impossible, to discriminate reliably between level ice and slightly ridged ice ($DIR = 2$). In these cases they usually chose the level ice category if the icebreaker reports did not indicate any difficulties for merchant ships. If this kind of difficulties were taking place, a ridged ice category was chosen.

Considering the contrast between level and ridged ice areas the situation changed gradually in February and March towards a more distinct separation between these ice types. We shall analyze the DIR charts separately for the period of strong thermodynamic growth (January, February) and more stable winter conditions (March) in Section 4.3 .

The examination of the monthly HV distributions, see Fig. 7, confirms our findings for the HH distribution. In January and February the values of σ^o_{HV} from level ice areas were close to the noise floor (-28dB) and, hence, too uninformative for a meaningful analysis. In the ridged areas σ^o_{HV} were $2 - 3$dB higher but still in general rather low indicating a low sea ice

The Cryosphere Discuss., https://doi.org/10.5194/tc-2017-127
Manuscript under review for journal The Cryosphere
Discussion started: 28 July 2017
© Author(s) 2017. CC BY 4.0 License.

surface roughness. In March the HV distributions both in level ice areas and ridged areas were on average about $1-2$dB higher than in the previous months. Also the contrast in the backscattering between ridged and level ice was more significant. As a consequence the σ^o_{HV} values affected the classification result in March but were not useful in the earlier months.

4.3 Classification results for several ridging categories

There was a fundamental imbalance between the sample sizes representing level ice and deformed ice classes. The samples from all the deformed ice classes formed about 40 % of the ice samples. If we had required that all the classes were of equal size in the training data, the amount of observations per ice category would have been low, e.g. less than 20 % of the level ice samples would have been utilized. When assessing the results we will keep in our mind the highly different sizes of the ice classes.

We run all our random forest classifications with the same set of tuning parameters for routine TreeBagger Matlab (2016). From the set of eight ($p = 8$) features we randomly chose $m = 4$ features to be used in a split. Often the value $m = \sqrt{p}$, i.e. $m = 3$ here, would have been recommended Hastie et. al. (2011). However, we noted that slightly better results were obtained with $m = 4$ for our data set. Another fixed option was that the minimum number of data points in the end nodes was set to ten. We grew 200 trees during the classification. Results with more decision trees did not yield any significant improvement of the error rates.

In first phase we investigated the capacity of the RF classifier to separate between level and deformed ice. Data of all the three months were included in the analyzed data set. The results are presented in Table 2. The overall classification rate was 82 % for the whole winter.

Next we examined the classification of all the four ridging categories through the three–month period. The training and test data sets had been selected from each month in our data set. The overall classification rate for the test period was 71%. Looking at the confusion matrix in Table 3 we can observe that the level ice category (93%) had a very high classification rate. The classification of the three categories for ridged ice was more challenging. The ridged ice clategory ($DIR = 3$) had a correct mode ice class (45%) but high misclassification rate (55%) and over 30% of the observations were confused with level ice. The slightly ridged ice ($DIR = 2$) was poorly distinguished. Only in the 15 % of the cases is was detected correctly. Most samples (42 %) were assigned to the level ice class which in the light of the previous discussion could be expected, i.e. the preference among the FIS ice analysts to use level ice category over slightly ridged ice in the manual ice charts. The ridged ice category with the most accurate classification rate (59 %) was the heavily ridged ice category $DIR = 4$.

To obtain more information on how the adopted approach works in rapidly changing ice conditions and on the other hand in more stable winter conditions we classified all three test months separately so that the training and testing data were collected during the same month. The overall accuracy of the monthly results varied largely being at its lowest in February (63 %), higher in January (83 %) and March (81 %). The corresponding Cohen's kappa figures were 0.60 (substantial agreement) , 0.52 (moderate agreement) and 0.68 (substantial agreement). The separation between all ice categories was easiest to perform in January (overall accuracy 83 %) where basically just three DIR categories appeared. An evidence that the definition of

© Author(s) 2017. CC BY 4.0 License.

different DIR categories were inconsistent with each other in January and February was that in these months the detection rate stayed below 100 % for the training data in the RF classification but it was 100 % for the March training data.

In each month level ice was the dominant ice category being over 50 % of all ice covered area. The DIR 2 category covered from 6 % to 19 % of the ice area depending on the month. In none of the months it was successfully detected due to its ambivalent definition with respect to the DIR 1 category. The DIR 3 category was successfully detected in January when its areal coverage was large (21 %) and in March when the boundaries between different ice categories were best defined during the test period. The heavily ridged ice fields (DIR=4) were usually well found except in January when such ridged areas were rare (about 1 %). A possible explanation for the lowest accuracy rate in February was that then the boundaries between different DIR regions were often visually rather difficult to discern in the SAR imagery according to our experience. Fig. 8 shows the variation of the detection rate for each DIR category in all the classification results. The most distinct feature in the results is the consistently poor detection rate for DIR 2.

In Fig. 9 we can see the Baltic Sea ice classification result (left) for a dual-pol pair of SAR mosaics from 9th of February 2013 (Fig. 2 top). Also the reference DIR chart is shown for comparison (bottom left). The automated DIR charts produced agreed well with the FIS ice charts for DIR values 1 and 3. However, the automated chart estimated a large fraction of DIR 2 category ice to DIR class 4. The DIR categories contained detailed markings of the cracks and openings in the central Bay of Bothnia which were detected by the SAR chart but not from the FIS chart. We remark that the SAR mosaic from 9th of February looked very similar to the one from 7th of February (two days earlier), when the same cracks / openings can be found, but the corresponding FIS ice chart DIR showed $DIR = 4$ in the areas to which was now assigned $DIR = 3$. This can be taken as an example of the subjectivity which is inherent to the manual ice charts.

There is a good overall agreement between the FIS chart and our DIR classification in Fig. 11. Most of the differences occur in the Bothnian Sea. There the FIS chart indicates mostly level ice and to some extent slightly ridged ice. On the other hand, the classification assigned to some FIS level ice areas the ridged ice and heavily ridged ice categories. Based on the SAR HH and HV images (see Fig. 10) those areas represent broken ice fields although the ridging intensity is hard to assess visually.

5 Discussion and Conclusions

For navigation in sea ice, the Degree of Ice Deformation parameter is one of the most useful parameters, even for the less experienced ship captains, because it is basically indicating if a vessel can pass or not through a block of ice, by knowing also the ship's characteristics. Subsequently, the DIR can function as a practical approximation for the more general Risk index Outcome (RIO) IMO (2016) for vessels operating in ice, when the existing ice parameters available are not sufficient (e.g. ice thickness, concentration). We have showed here that the DIR parameter can be estimated rather well using the SAR texture features and ice concentration when compared to the values extracted from the manually prepared FIS ice charts. The used features describe versatile statistics of σ^o variation in the SAR imagery. The DIR classification is a suitable operation for a SAR based approach because the C-band SAR is sensitive to the large scale surface roughness, i.e ridging.

© Author(s) 2017. CC BY 4.0 License.

Our first goal was to discriminate between ridged ice areas and level ice. This objective was reached with high accuracy (82 %). The more ambitious goal to estimate the different DIR categories succeeded reasonably well. Especially the estimation procedure worked well in midwinter when the ice conditions were stable and sea ice at its thickest. The promising results in the DIR estimation are important because our field campaign data demonstrated that the FIS DIR numeral serves as an efficient indicator between the relative ridge density classes.

When we consider the purpose of the ice charts one significant factor must be considered. This is that in the ice infested areas two types of ships proceed: ships with the assistance of an icebreaker or independently proceeding ships. In the Baltic Sea most of the merchant ships need the icebreaker assistance. Ships of the highest ice class, 1A Super, are designed to operate in difficult ice conditions independently. The FIS ice charts are targeted to the ships which advance in difficult ice conditions as a convoy following the icebreaker. Based on the discussions with the ice analysts the following remark can be made: if the ice conditions do not pose a realistic risk for icebreakers to get stuck, in the FIS ice charts they are often assigned to smaller degree of ice riding, even if these same areas may exhibit a considerable obstacle for independent ships. Hence, the availability of the icebreaker assistance affects the DIR classifications in the FIS ice charts.

The primary objective of our classification algorithm is to separate the severe ice conditions from the easier ice conditions. To reach this goal it relies only on the SAR statistics. In some cases this may lead to differences between the FIS ice charts and our classification results because the FIS charts take into account the icebreaker factor not seen in the SAR imagery. Hence, these two data sets can be interpreted from slightly different perspectives. An example of this difference is our earlier discussion related to Fig. 10. As we noticed there were ice areas in the Bothnian Sea areas marked as slightly ridged ice (DIR=2) in the FIS DIR chart, whereas our automated DIR chart showed higher degree of ridging for these areas. Our estimates closely followed the SAR features and the deformed ice areas are indicated in our DIR chart unlike in the FIS chart. The mentioned ridged areas very likely would not be difficult to break by an icebreaker. Thus, they are assigned in the FIS chart to the DIR 2 category. If we consider a weaker vessel trying to pass independently through the same areas, the automated chart would be more informative, showing more accurately the passages which are difficult or easy to navigate. One essential advantage of the automated DIR charts over the FIS charts is that leads and small level ice areas between ridged ice zones are present in these charts but typically not in the FIS charts.

Before setting up an operational detector for the Baltic Sea area, we need to test our algorithm with at least two more winters data and optimize it for the best possible result. In an operational mode we can add to our training data the SAR/FIS IC data collected during days before the day FIS prepares its ice chart. The freshest classification result available for FIS is the DIR classification based on the SAR and the FIS IC data from the previous day. This should improve the classification accuracy of the DIR chart. Currently our training data rely on older data.

Our algorithm can be extended for use in Arctic Ocean, where there is a higher demand for reliable ice information on prevailing ice conditions, and icebreaker assistance often not available in a reasonable time. By having an automated DIR chart utilizing the fine resolution (100 m or less) SAR data and qualitatively presenting the suitability of the ice conditions for navigation, would be a remarkable gain for Arctic shipping. E. g. in the Kara Sea year-round shipping will significantly increase in the coming years through the high volume liquefied natural gas (LNG) production in the Yamal Peninsula. For Arctic sea

© Author(s) 2017. CC BY 4.0 License.

areas, however, the algorithm would be more difficult to validate without having knowledge of the true areal DIR values. The current Russian Ice Charts contain only the general WMO sea ice classes without any indication of degree of ridging. Perhaps the regional sea ice model implemented for the Kara Sea (Dr. Andrea Gierisch, private communication) will be helpful in the development of an automated classifier. One alternative is also to use the Baltic Sea ice data as a first trial to train the algorithm for the Arctic conditions.

Data availability. All data can be obtained by contacting the first author.

Author contributions. The concept of the study was conceived by AG, JK and MS. The SAR processing was done and reported jointly by JK and AG. MM commented the SAR processing. The statistical analysis was performed and written by MS. ML analyzed and wrote about the 2011 field data. MM and AG wrote the introduction. AG and MS wrote the conclusion section. JV commented the results and the conclusions from the point of view of an ice analyst. All authors contributed to the editing of the text

Competing interests. The authors declare that they have no competing interest.

Acknowledgements. The work of Alexandru Gegiuc, Juha Karvonen and Marko Mäkynen was supported by Space-borne observations for detecting and forecasting sea ice cover extremes (SPICES) funded by the European Union's Horizon 2020 Programme (Grant Agreement No. 640161). Markku Similä and Mikko Lensu were supported by the KAMON project funded by Academy of Finland (contract 283034) and the BONUS STORMWINDS project funded jointly by the EU and the Academy of Finland (contract 291683)

© Author(s) 2017. CC BY 4.0 License.

References

Barber, D. G. and LeDrew, E. F.: SAR sea ice discrimination using texture statistics: A multivariate approach. Photogr. Eng. and Remote Sensing, 57, 385-395, 1991.

Berthod, M., Kato, Z., Yu, S., Zerubia, J.: Bayesian image classification using Markov random fields, Image and Vision Computing, 14, 285-295, 1996.

Besag, J.: Spatial Interaction and the Statistical Analysis of Lattice Systems, J. Royal Statistical Society, Series B, 36, 192–236, 1974.

Breiman, L.: Random forests, Machine Learning, 24, 5–32, 2001.

Canadian Ice Service, MANICE, Manual of Standard Procedures for Observing and Reporting Ice Conditions, Revised Ninth Edition, June 2005.

Canny, J.: A Computational Approach to Edge Detection, IEEE Trans. Pattern Analysis and Machine Intelligence, 8, 679 - 698, 1986.

Carlstrom, A., Ulander, L. M. H.: Validation of Backscatter Models for Level and Deformed Sea Ice in ERS-1 SAR Images, Int. J. Remote Sens., 16, 3245-3266, 1995.

Calström, A., Ulander, L. M. H.: C-band backscatter signatures of old sea ice in the central Arctic during freeze-up. IEEE Trans. Geoscience and Remote Sensing, 31, 819-829, 1995.

Cerny, V.: Thermodynamical approach to the traveling salesman problem: An efficient simulation algorithm, J. Optimization Theory and Applications, 45, 41–51, 1985.

Clausi, D. A.: Comparison and fusion of co-occurrence, Gabor, and MRF texture features for classification of SAR sea ice imagery, Atmos. Ocean, 39, 183–194, 2001.

Clausi, D. A., Qin, A. K., Chowdhury, M. S., Yu, P., Maillard, P.: MAGIC: MAp-Guided Ice Classification System, Can. J. Remote Sensing, 36, S13-S25, 2010.

Dempster, A. P., Laird, N. M., Rubin, D. B.: Maximum Likelihood from Incomplete Data via the EM Algorithm, J. Royal Statistical Society Series, 39, pp. 1-38, 1977.

Deng, H., Clausi, D. A.: Gaussian MRF rotation- invariant features for image classification, IEEE Trans. Pattern Analysis and Machine Intelligence, 26, 7, 951-955, 2004.

Deng, H., Clausi, D. A.: Unsupervised segmentation of synthetic aperture radar sea ice imagery using a novel Markov random field model, IEEE Trans. Geoscience and Remote Sensing, 43, 528-538, 2005.

Dierking, W., Pettersson, M. I., Askne, J.: Multifrequency scatterometer measurements of Baltic Sea ice during EMAC-95, Int. J. Remote Sens., 20, 349–372, 1999.

Efron, B. and Tibshirani, R., An Introduction to the Bootstrap, Chapman and Hall, London, 1993.

Haas, C., Lobach, J., Hendricks, S., Rabenstein, L., Pfaffling, A.: Helicopter-borne measurements of sea ice thickness, using a small and lightweight, digital EM system, J. Applied Geophysics, 67, 234-241, 2009.

Hallikainen, M.: Microwave remote sensing of low-salinity sea ice., In F. Carsey (Ed.), Microwave Remote Sensing of Sea Ice (pp. 361-373). Washington D.C.: AGU, 1992.

Hastie, T., Tibshirani, R., Friedman, J. , The Elements of Statistical Learning, 2nd ed., Springer, New York, 2011.

International Maritime Organisation (IMO), MSC.1/Circ.1519, June, 2016.

Lindsay, R. W., Zhang, J., Rothrock, D. A.: Sea-ice deformation rates from satellite measurements and in a model, Atmos. Ocean, 41, 1-21, 2003.

© Author(s) 2017. CC BY 4.0 License.

Karvonen, J.: Baltic Sea Ice SAR Segmentation and Classification Using Modified Pulse-Coupled Neural Networks, IEEE Trans. Geoscience and Remote Sensing, 42, 1566-1574, 2004.

Karvonen, J.: Evaluation of the operational SAR based Baltic Sea ice concentration products. Adv. Space Res. 56, 119-132, 2015.

Karvonen, J., Similä, M., Mäkynen, M.: Open Water Detection from Baltic Sea Ice Radarsat-1 SAR Imagery, IEEE Geoscience and Remote Sensing Letters, 2, 275-279, 2005.

Kirkpatrick, S., Gelatt Jr, C. D., Vecchi, M. P.: Optimization by Simulated 220, 671–680, 1983.

Kankaanpää, P., Distribution, morphology and structure of sea ice pressure ridges in the Baltic Sea. Fennia-International Journal of Geography, 175, 139-240, 1997.

Kato, Z.: Multi-scale Markovian Modelisation in Computer Vision with Applications to SPOT Image Segmentation, PhD thesis, INRIA Sophia Antipolis, France, 1994.

Kato, Z., Zerubia, J., Berthod, M.: Satellite image classification using a modified Metropolis dynamics, Proc. IEEE International Conf. on Acoust., Speech and Sig. Proc., 3, 573-576, San Francisco, CA, March 23-26, 1992.

Leigh, S., Wang, Z., Clausi, D.: Automated Ice–Water Classification Using Dual Polarization SAR Satellite Imagery, IEEE Trans. Geoscience and Remote Sensing, 52, 5529-5539, 2014.

Lensu, M.: The evolution of ridged ice fields. Helsinki University of Technology, Ship Laboratorty report series M-280.

Leppäranta, M., Hakala, R.: The structure and strength of first-year ice ridges in the Baltic Sea., Cold Reg. Sci. Tech., 20, 295-311, 1992.

Lewis, J. E., Leppäranta, M., and Granberg, H. B.: Statistical properties of sea ice surface topography in the Baltic Sea. Tellus A, 45, 127–142, 1993.

Maillard, P., Clausi, D. A., Deng, H.: Map-guided sea ice segmentation and classification using SAR imagery and a MRF segmentation scheme, IEEE Trans. Geoscience and Remote Sensing, 43, 2940-2951, 2005.

MATLAB and Statistics Toolbox Release 2016a, The MathWorks, Inc., Natick, Massachusetts, United States.

MDA (MacDonald, Dettwiler and Associates, Ltd.), Radarsat-2 product description, Tech. Rep. RN-SP-52-1238, Issue 1/11, MDA, BC, Canada, pp. 84., May 5, 2014.

Mäkynen, M., Manninen, T., Similä, M., Karvonen, J., Hallikainen, M.: Incidence Angle Dependence of the Statistical Properties of the C-Band HH-Polarization Backscattering Signatures of the Baltic Sea Ice, IEEE Tans. Geoscience and Remote Sensing, 40, 2593-2605, 2002.

Mäkynen, M., Hallikainen, M.: Investigation of C- and X-band backscattering signatures of the Baltic Sea ice., Int. J. Remote Sens., 25, 2061–2086, 2004.

Metropolis, N., Rosenbluth, A. W., Rosenbluth, M. N., Teller, A. H., Teller, E.: Equation of State Calculations by Fast Computing Machines, J. Chemical Physics, 21, 1087, 1953.

Ochilov, S., Clausi, D. A.: Operational SAR Sea-Ice Classification, IEEE Trans. Geoscience and Remote Sensing, 50, 11, 4397–4408, 2012.

Palosuo, E., Leppäranta, M., Seinä, A.: Formation, thickness and stabity of fast ice along the Finnish coast., Res. Rep. 36, Winter Navig. Res. Board, Helsinki, Finland, 1982.

Rao, C. R.: The utilization of multiple measurements in problems of biological classification, J. Royal Statistical Society, Series B, 10, 159–203, 1948.

Ripley, B. D.: Pattern Recognition and Neural Networks, Cambridge University Press, 1996.

Rue, H., Held, L.: Gaussian Markov Random Fields: Theory and Applications, CRC Press, 2005.

© Author(s) 2017. CC BY 4.0 License.

Sandven, S., Alexandrov, V., Zakhvatkina, N., Babiker, M.: Sea ice classification using Radarsat-2 dual-polarisation data, Proc ESA SeaSAR 2012, SP-709, 2012.

A. Seinä, A., Palosuo, E.: The classification of the maximum annual extent of ice cover in the Baltic Sea 1720-1995., Meri Report No. 27, 79-91, Finnish Institute of Marine Research, Finland, 1996.

Seinä, A., Peltola, J.: Duration of ice season and statistics of fast ice thickness along the Finnish coast 1961-1990., Finnish Marine Research Report 258, 1-46, Finnish Institute of Marine Research, Finland, 1991.

Shannon, C.E.: A Mathematical Theory of Communication, The Bell System Technical Journal, 27, 379–423, 623–656, 1948.

Similä, M.: SAR image segmentation by a two-scale contextual classifier, Proc. SPIE Conf. Image and Signal Proc. for Remote Sensing, v. 2315, Ed. J. Desachy, 434–443, 1994.

Similä, M., Arjas, E., Mäkynen, M., Hallikainen, M. T.: A Bayesian classification model for sea ice roughness from scatterometer data, IEEE Trans. Geoscience and Remote Sensing, 39, 7, 1586-1595, 2001.

Similä, M., Mäkynen, M., Heiler, I.: Comparison between C band synthetic aperture radar and 3-D laser scanner statistics for the Baltic Sea ice.J. Geophys. Res. Oceans, 115, C10056, 2010.

Shokr, M.: Compilation of a radar backscatter database of sea ice types and open water using operational analysis of heterogeneous ice regimes, Can. J. Remote Sensing, 35, 369-384, 2009.

Soh, L.-K., Tsatsoulis, C.: Texture analysis of SAR sea ice imagery using gray level co-occurrence matrices, IEEE Trans. Geoscience and Remote Sensing, 37, 780-795, 1999.

Soh, L. K., Tsatsoulis, C., Gineris, D., Bertoia, C.: ARKTOS: an intelligent system for SAR sea ice image classification, IEEE Trans. Geoscience and Remote Sensing, 42, 229-248, 2004.

Souyris, J.-C., Imbo, P., Fjortoft, R., Mingot, S., Lee, J.-S.: Compact polarimetry based on symmetry properties of geophysical media: the *pi*/4 mode, IEEE Trans. on Geoscience and Remote Sensing, 43, 3, 634–646, 2005.

Strong, C.: Atmospheric influence on Arctic marginal ice zone position and width in the Atlantic sector, February-April 1979-2010, Clim. Dynam., 39, 12, 3091-3102, 2012.

Wessel, P. and Smith W.H.F.: A global self-consistent, hierarchical, high-resolution shoreline database. J. Geophys. Res., 101, 8741-8743, 1996.

WMO Sea ice Nomenclature, WMO n. 259 (rev, 2010), 2010.

Yu, Q., Clausi, D. A.: SAR sea-ice image analysis based on iterative region growing using semantics, IEEE Trans. Geoscience and Remote Sensing, 45, 3919-3931, 2007.

The Cryosphere Discuss., https://doi.org/10.5194/tc-2017-127
Manuscript under review for journal The Cryosphere
Discussion started: 28 July 2017
© Author(s) 2017. CC BY 4.0 License.

Table 1. Comparison of ridge statistical parameters with ice chart degrees of ice ridging.

DIR	3	4
Number of cells [km^2]	590	1079
Ridge sail height [m]	0.61	0.61
Ridge density [1/km]	12.7	21.5
Total thickness [m]	0.76	1.08

The Cryosphere Discuss., https://doi.org/10.5194/tc-2017-127
Manuscript under review for journal The Cryosphere
Discussion started: 28 July 2017
© Author(s) 2017. CC BY 4.0 License.

Table 2. Confusion matrix for the level ice vs. ridged ice classification for the test period.

FMI	Sample size	Ice category	
Ice cateogory	N	level	ridged
level	59 %	**87 %**	13 %
ridged	41 %	24 %	**76 %**

The Cryosphere Discuss., https://doi.org/10.5194/tc-2017-127
Manuscript under review for journal The Cryosphere
Discussion started: 28 July 2017
© Author(s) 2017. CC BY 4.0 License.

Table 3. Confusion matrix for the RF classification for the test period.

FMI	sample size	RF classes			
DIR	N	1	2	3	4
1	59 %	**93 %**	1 %	4 %	2 %
2	14 %	**42 %**	15 %	28 %	15 %
3	15 %	32 %	5 %	**45 %**	18 %
4	12 %	18 %	3 %	20 %	**59 %**

The Cryosphere Discuss., https://doi.org/10.5194/tc-2017-127
Manuscript under review for journal The Cryosphere
Discussion started: 28 July 2017
© Author(s) 2017. CC BY 4.0 License.

Table 4. Confusion matrix for the RF classification in January

FMI	sample size	RF classes			
DIR	N	1	2	3	4
1	72 %	**94 %**	2 %	4 %	0 %
2	6 %	**48 %**	15 %	36 %	0 %
3	21 %	35 %	1 %	**64 %**	0 %
4	1 %	**47 %**	0 %	21 %	32%

The Cryosphere Discuss., https://doi.org/10.5194/tc-2017-127
Manuscript under review for journal The Cryosphere
Discussion started: 28 July 2017
© Author(s) 2017. CC BY 4.0 License.

Table 5. Confusion matrix for the RF classification in February

FMI	sample size	RF classes			
DIR	N	1	2	3	4
1	55 %	**92 %**	1 %	5 %	2 %
2	19 %	**46 %**	13 %	21 %	20 %
3	17 %	21 %	6 %	29 %	**44 %**
4	9 %	18 %	16 %	16 %	**51 %**

The Cryosphere Discuss., https://doi.org/10.5194/tc-2017-127
Manuscript under review for journal The Cryosphere
Discussion started: 28 July 2017
© Author(s) 2017. CC BY 4.0 License.

Table 6. Confusion matrix for the RF classification in March

FMI	sample size	RF classes			
DIR	N	1	2	3	4
1	59 %	**92 %**	4 %	2 %	2 %
2	9 %	16 %	**32 %**	21 %	31 %
3	10 %	44 %	4 %	**51 %**	1 %
4	22 %	4 %	2 %	6 %	**88 %**

The Cryosphere Discuss., https://doi.org/10.5194/tc-2017-127
Manuscript under review for journal The Cryosphere
Discussion started: 28 July 2017
© Author(s) 2017. CC BY 4.0 License.

Figure Captions

Figure 1. Example of RS-2 dual polarized SAR image mosaic (left: HH, middle HV) over the Baltic Sea on 15 March 2013 and the corresponding DIR chart (right) showing manually drawn polygons of different degrees of ice ridging, including the marginal ice zone detection mask based on ice concentration values between 25% and 80% and open-water mask based on ice concentration values smaller than 25%.

Figure 2. Example of RS2 SAR data from 9th of February 2013 in HH (top left) and HV (top right) polarizations together with the segmentation result (bottom left) and the Ice Concentration Chart.

Figure 3. Example of SAR features computed for central BOB. a-b) original SAR in 500m resolution; c) Segmentation result of the first principal component of the original HH and HV SAR channels; d) FIS SIC (1-100%); e)FIS DIR (1-4); f-g)segment means; h) AC_{HH}; i)AC_{HV}; j)E_{HH}; k)E_{HV}; l) CV_{HH}; m)CV_{HV}; n)ED_{HH}; o)ED_{HV}; p)K_{HH}; q)K_{HV}.

Figure 4. The importance of different features when the training data covered the whole test period. The order of the features is: AC_{HH}, IC, ED_{HH}, E_{HH}, K_{HH}, σ^o_{HH}, CV_{HH}, σ^o_{HV} , see text for explanations.

Figure 5. Ridge density variation in the test area (upper panel, left), HEM thickness measurements (upper panel, right), DIR indices (lower panel, left), ridge density histogram in one 1x1 NM cell (lower panel, right).

Figure 6. The monthly HH distribution for level (dashed line) and ridged (solid line) ice areas. The results are for January (left), February (middle), March (right) in 2013.

Figure 7. The monthly HV distribution for level (dashed line) and ridged (solid line) ice areas. The results are for January (left), February (middle), March (right) in 2013.

Figure 8. The detection rates for the different DIR categories in all the classification.

Figure 9. Degree of Ice Ridging extracted from the digitized Finnish Ice Charts (bottom left) and the result of estimated DIR based on our RF approach. The DIR charts includes the marginal ice zones (25%<IC<80%) extracted from the Ice Concentration charts (see Fig. 2).

Figure 10. Example of RS2 SAR data from 15th of March 2013 in HH (top left) and HV (top right) polarizations. Middle left: MRF MMD Segmentation result for the HH-HV PCA component. Middle right: Ice Concentration Chart extracted from the Finnish Ice Chart.

Figure 11. Degree of Ice Ridging extracted from the digitized Finnish Ice Charts Bottom right: Result of Estimated DIR based on our RF approach. The DIR charts includes the marginal ice zones (25%<IC<80%) extracted from the Ice Concentration charts (see Fig. 10).

The Cryosphere Discuss., https://doi.org/10.5194/tc-2017-127
Manuscript under review for journal The Cryosphere
Discussion started: 28 July 2017
© Author(s) 2017. CC BY 4.0 License.

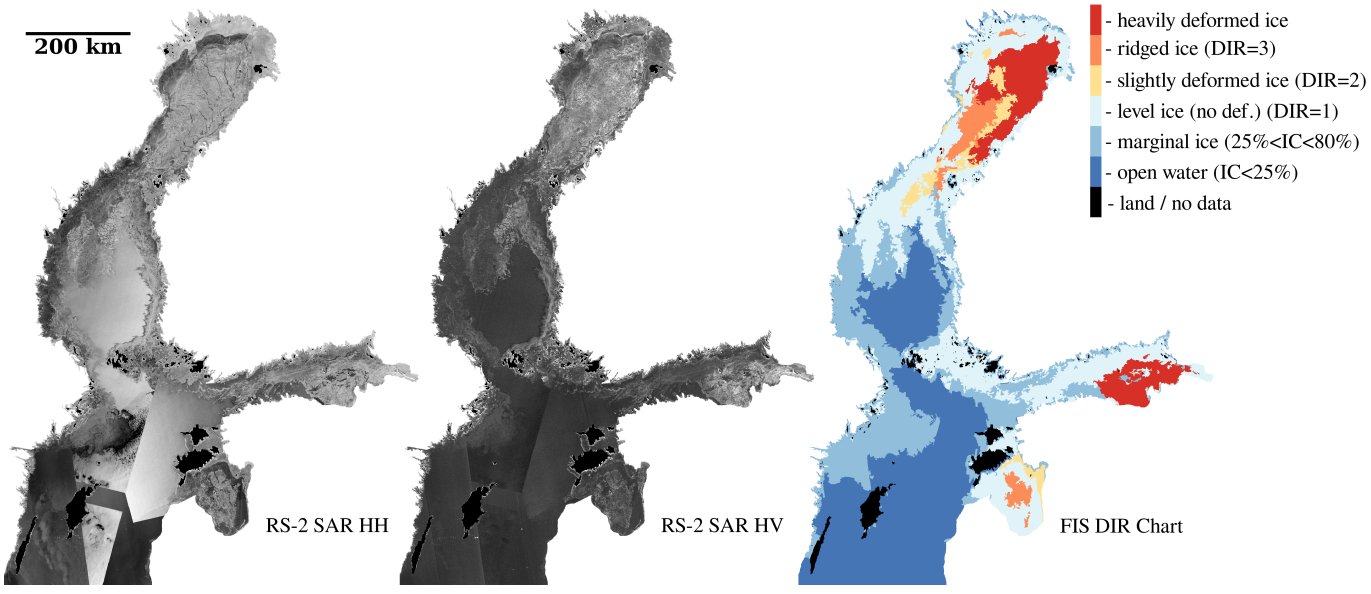

Figure 1. Example of RS-2 dual polarized SAR image mosaic (left: HH, middle HV) over the Baltic Sea on 15 March 2013 and the corresponding DIR chart (right) showing manually drawn polygons of different degrees of ice ridging, including the marginal ice zone detection mask based on ice concentration values between 25% and 80% and open-water mask based on ice concentration values smaller than 25%.

The Cryosphere Discuss., https://doi.org/10.5194/tc-2017-127
Manuscript under review for journal The Cryosphere
Discussion started: 28 July 2017
© Author(s) 2017. CC BY 4.0 License.

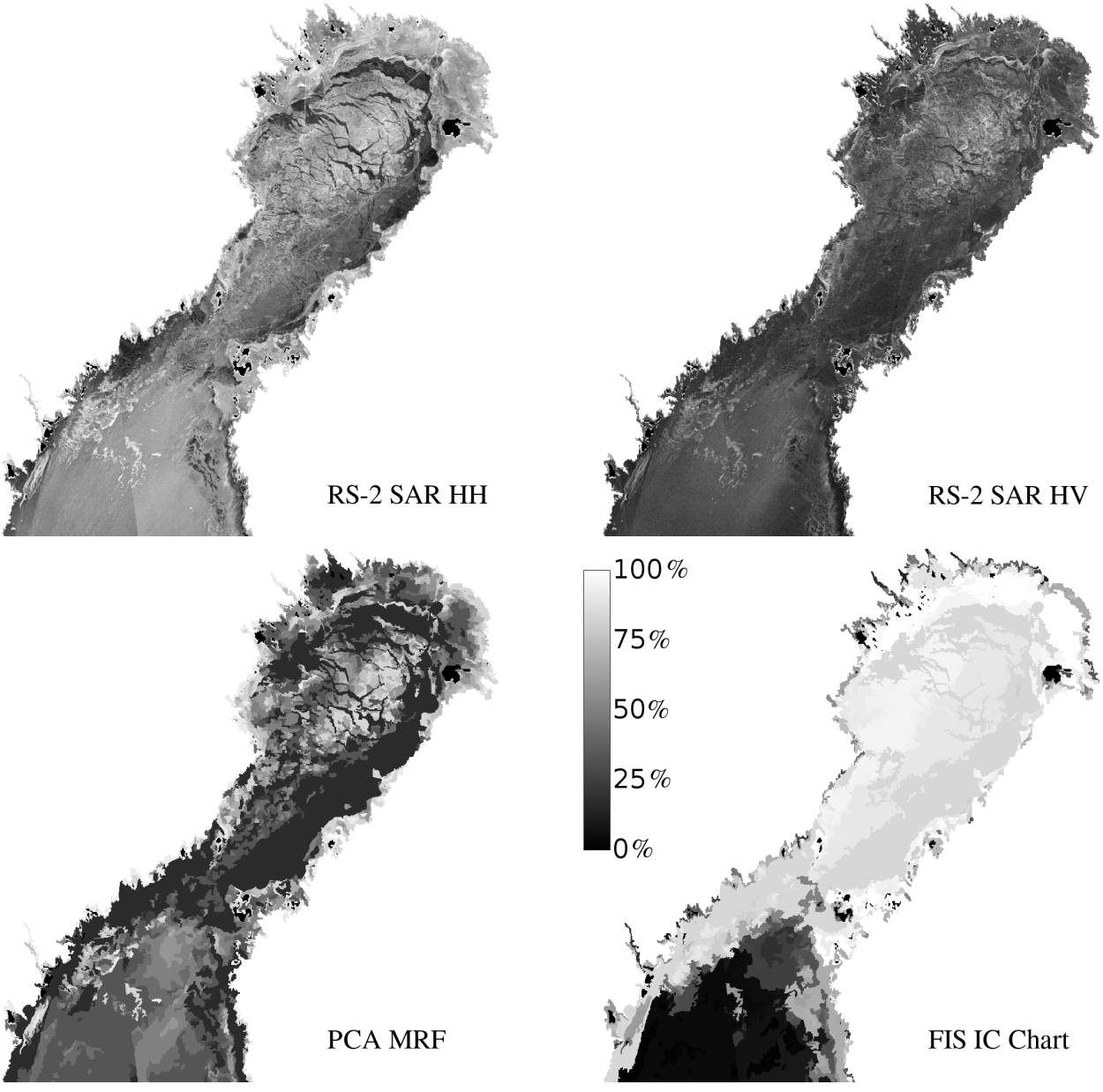

Figure 2. Example of RS2 SAR data from 9th February 2013 in HH (top left) and HV (top right) polarizations together with the segmentation result (bottom left) and the Ice Concentration Chart.

The Cryosphere Discuss., https://doi.org/10.5194/tc-2017-127
Manuscript under review for journal The Cryosphere
Discussion started: 28 July 2017
© Author(s) 2017. CC BY 4.0 License.

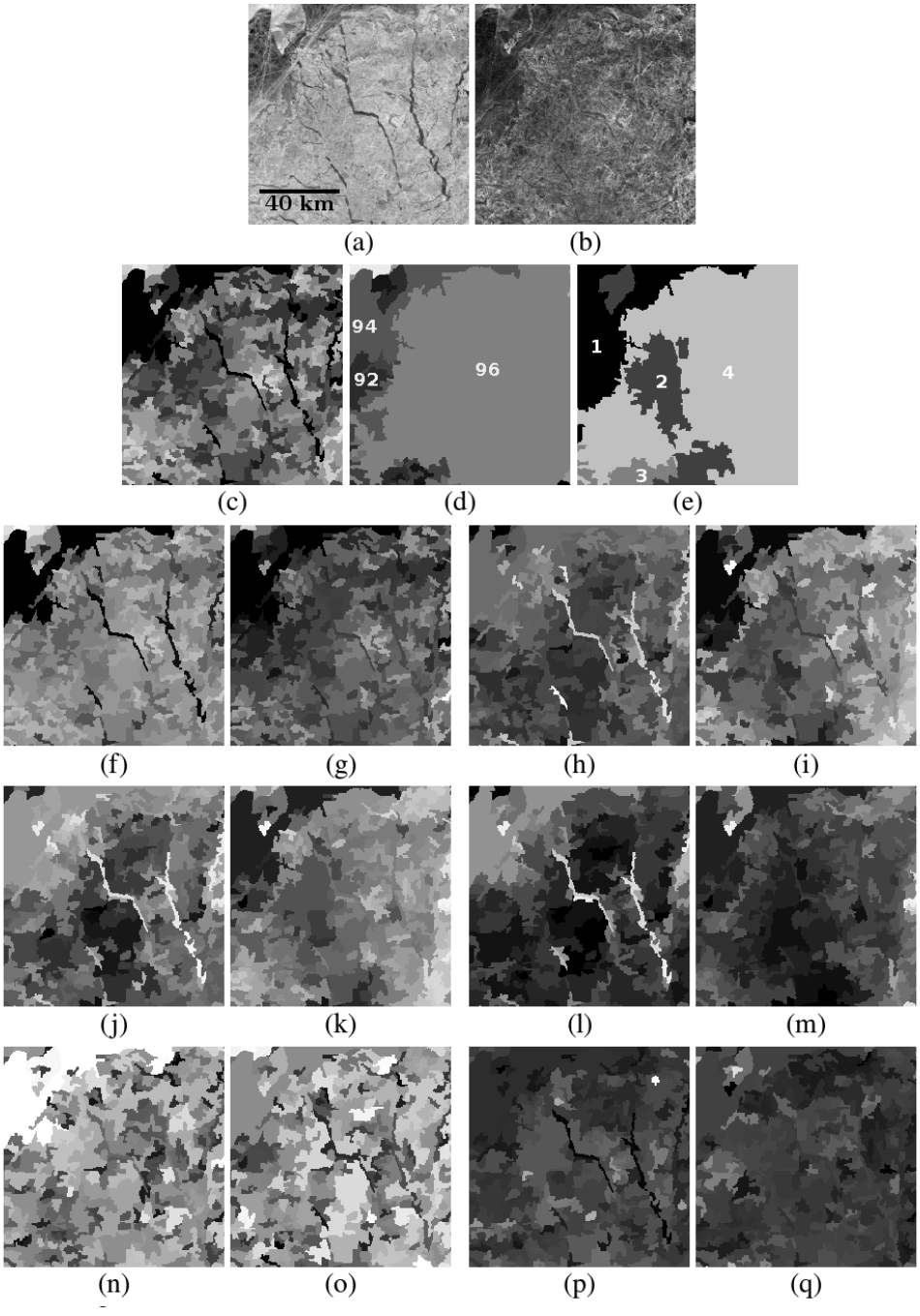

Figure 3. Example of SAR features computed for central BOB. a-b) original SAR HH and HV in 500m resolution; c) Segmentation result of the first principal component of the original HH and HV SAR channels; d) FIS SIC (1-100%); e)FIS DIR (1-4); f-g)segment means; h) AC_{HH}; i)AC_{HV}; j)E_{HH}; k)E_{HV}; l) CV_{HH}; m)CV_{HV}; n)ED_{HH}; o)ED_{HV}; p)K_{HH}; q)K_{HV}.

The Cryosphere Discuss., https://doi.org/10.5194/tc-2017-127
Manuscript under review for journal The Cryosphere
Discussion started: 28 July 2017
© Author(s) 2017. CC BY 4.0 License.

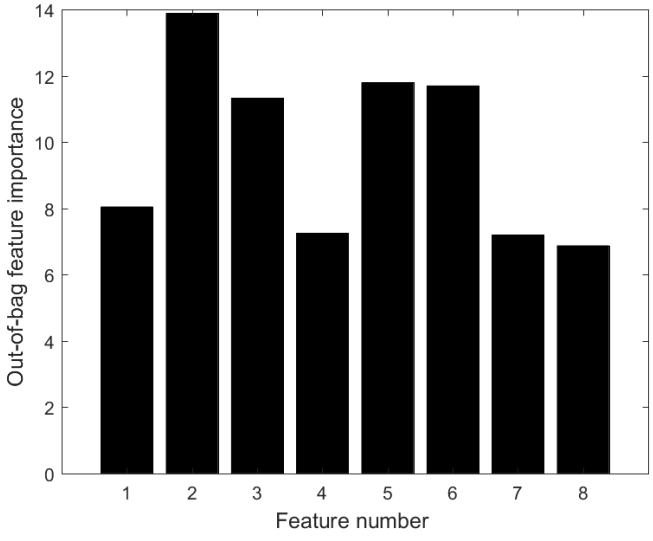

Figure 4. The importance of different features when the training data covered the whole test period. The order of the features is: AC_{HH}, IC, ED_{HH}, E_{HH}, K_{HH}, σ^o_{HH}, CV_{HH}, σ^o_{HV} , see text for explanations.

The Cryosphere Discuss., https://doi.org/10.5194/tc-2017-127
Manuscript under review for journal The Cryosphere
Discussion started: 28 July 2017
© Author(s) 2017. CC BY 4.0 License.

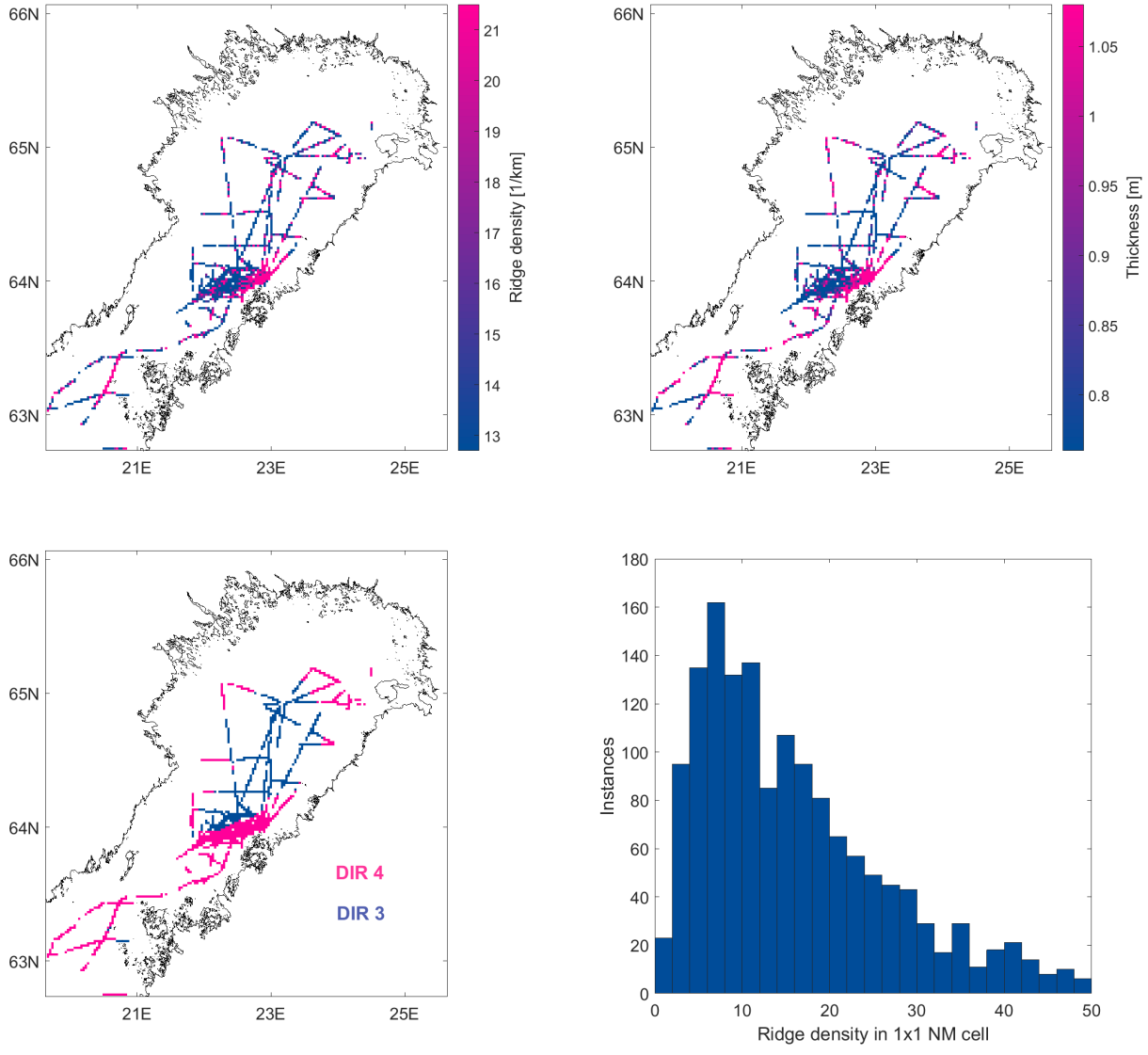

Figure 5. Ridge density variation in the test area (upper panel, left), HEM thickness measurements (upper panel, right), DIR indices (lower panel, left), ridge density histogram in one 1x1 NM cell (lower panel, right).

The Cryosphere Discuss., https://doi.org/10.5194/tc-2017-127
Manuscript under review for journal The Cryosphere
Discussion started: 28 July 2017
© Author(s) 2017. CC BY 4.0 License.

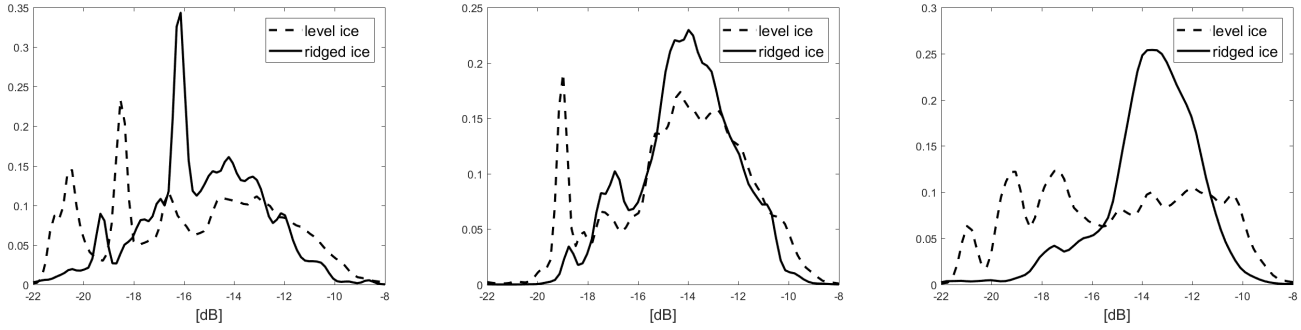

Figure 6. The monthly HH distribution for level (dashed line) and ridged (solid line) ice areas. The results are for January (left), February (middle), March (right) in 2013.

The Cryosphere Discuss., https://doi.org/10.5194/tc-2017-127
Manuscript under review for journal The Cryosphere
Discussion started: 28 July 2017
© Author(s) 2017. CC BY 4.0 License.

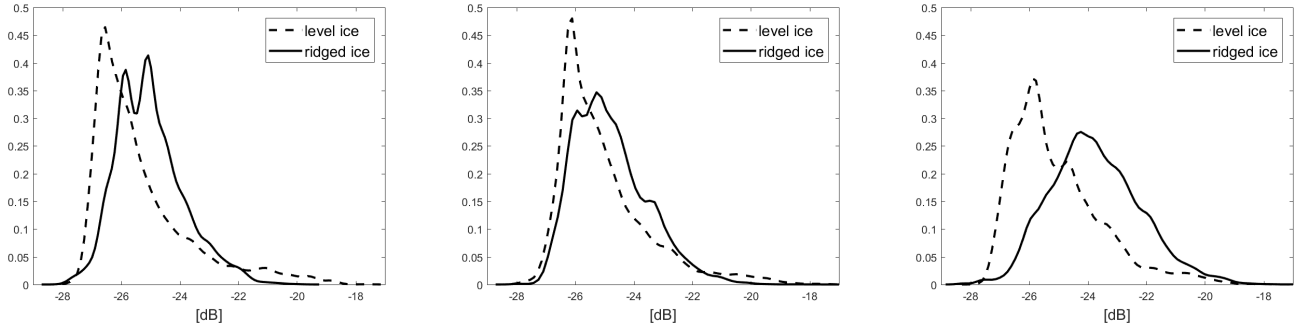

Figure 7. The monthly HV distribution for level (dashed line) and ridged (solid line) ice areas. The results are for January (left), February (middle), March (right) in 2013.

The Cryosphere Discuss., https://doi.org/10.5194/tc-2017-127
Manuscript under review for journal The Cryosphere
Discussion started: 28 July 2017
© Author(s) 2017. CC BY 4.0 License.

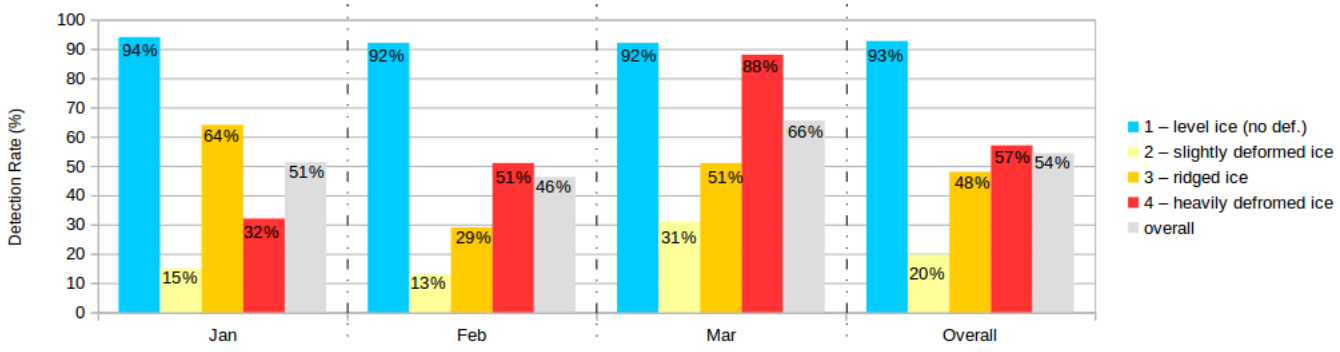

Figure 8. The detection rates for the different DIR categories in all the classification.

The Cryosphere Discuss., https://doi.org/10.5194/tc-2017-127
Manuscript under review for journal The Cryosphere
Discussion started: 28 July 2017
© Author(s) 2017. CC BY 4.0 License.

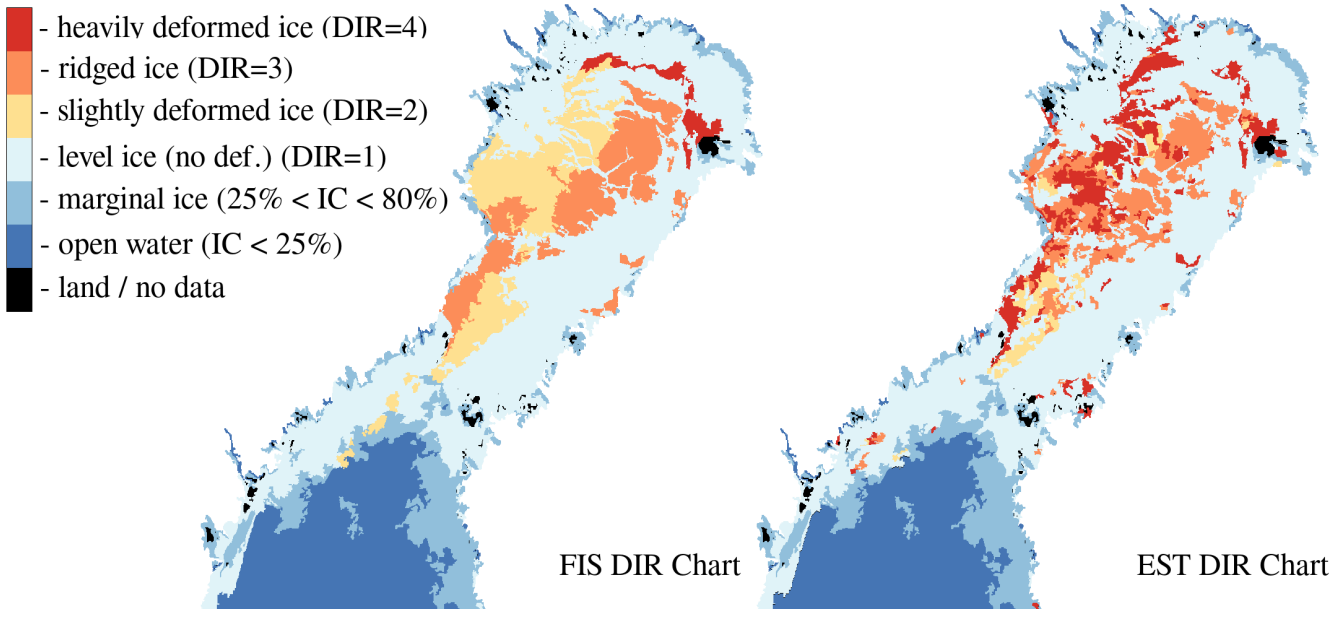

Figure 9. Degree of Ice Ridging extracted from the digitized Finnish Ice Charts on 9th February 2013 (left) and the result of estimated DIR based on our RF approach (right). The DIR charts includes the marginal ice zones (25%<IC<80%) extracted from the Ice Concentration charts (see Fig. 2).

The Cryosphere Discuss., https://doi.org/10.5194/tc-2017-127
Manuscript under review for journal The Cryosphere
Discussion started: 28 July 2017
© Author(s) 2017. CC BY 4.0 License.

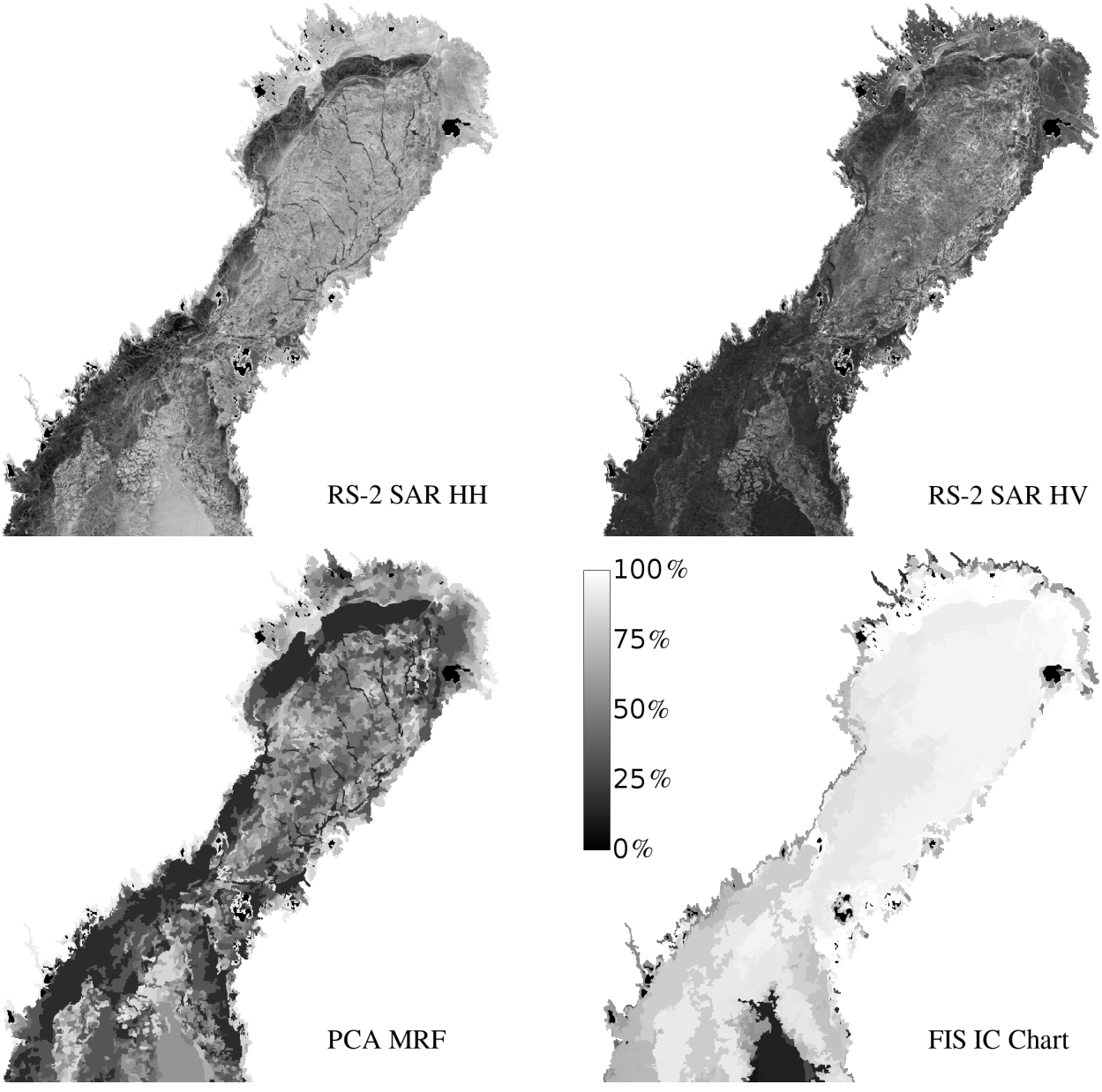

Figure 10. Example of RS2 SAR data on 15th March 2013 in HH (top left) and HV (top right) polarizations. Middle left: MRF MMD Segmentation result for the HH-HV PCA component. Middle right: Ice Concentration Chart extracted from the Finnish Ice Chart.

The Cryosphere Discuss., https://doi.org/10.5194/tc-2017-127
Manuscript under review for journal The Cryosphere
Discussion started: 28 July 2017
© Author(s) 2017. CC BY 4.0 License.

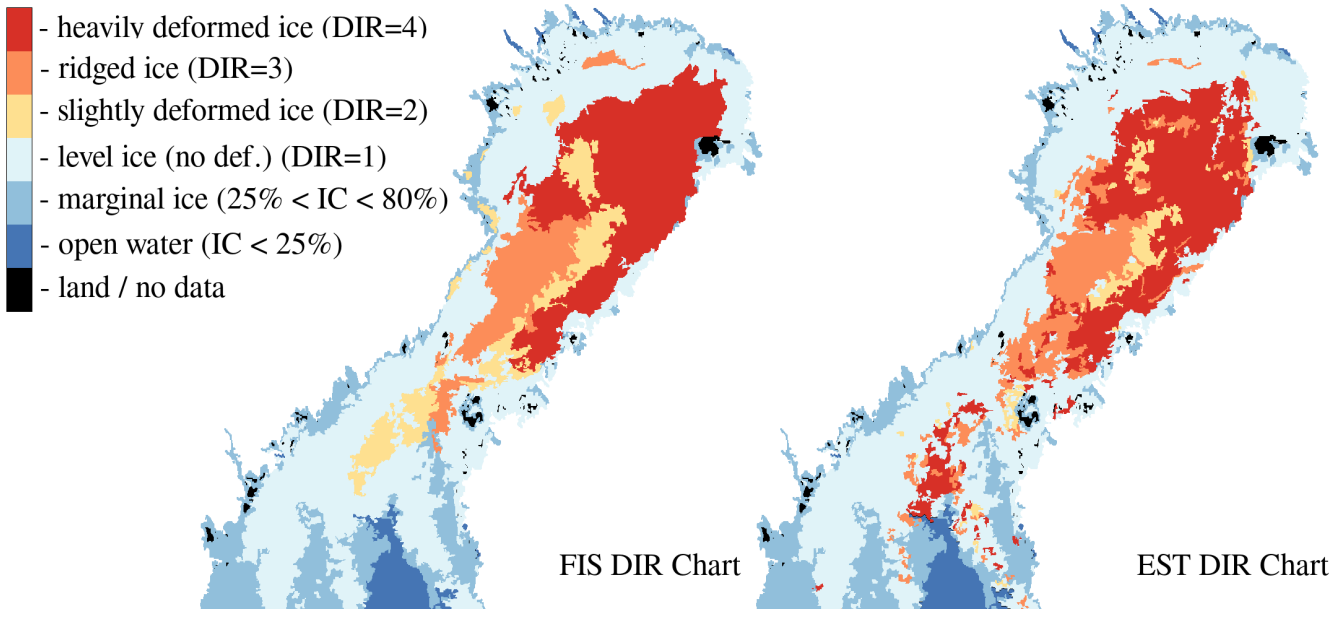

Figure 11. Degree of Ice Ridging extracted from the digitized Finnish Ice Charts on 15th March 2013 (left); Result of Estimated DIR based on our RF approach (right). The DIR charts includes the marginal ice zones (25%<IC<80%) extracted from the Ice Concentration charts (see Fig. 10).